PHOTOTHERMAL EVALUATION OF DIFFUSION COATINGS

N. Gopalsami, D. N. Rose†, R. A. Roberts, and W. A. Ellingson

Materials and Components Technology Division
Argonne National Laboratory
Argonne, Illinois 60439

†U. S. Army Tank-Automotive Command, AMSTA-RSA
Warren, Michigan 48397-5000

INTRODUCTION

Chromized and chrome-aluminized coatings, applied to 2.25 Cr-1 Mo and 9 Cr-1 Mo steel substrates by a pack-diffusion process, are being considered for advanced heat exchanger (heat recovery) systems of coal gasifiers [1]. The materials used in this application must have good corrosion resistance and high mechanical strength for prolonged operation at high temperatures (up to 650°C) in the presence of aggressive gas mixtures. The combination of coatings of oxide-forming elements such as Cr and Aℓ (which protect against corrosion) and low-alloy steels (which provide mechanical strength) is economically attractive. The pack-diffusion process is well suited to the application of these coatings to large, complex-shaped components of heat exchangers.

Nondestructive evaluation (NDE) methods must be developed for characterization of as-received coatings relative to acceptance criteria, and for field inspection. A candidate NDE technique should be capable of detecting fine cracks, inclusions, voids, and Cr/Aℓ concentration profiles [2]. The defect sizes are on the order of tens of micrometers and therefore require high spatial resolution. The NDE technique must be adaptable to complex (particularly tubular) surfaces and varying surface conditions (up to several tens of micrometers of surface roughness). Thermal-wave imaging technique reported in this paper was investigated because of its high resolution capability, generally noncontacting nature, and adaptability to complex surfaces.

PROBLEM DESCRIPTION AND ANALYSIS

The nature and complexity of the problem can be explained with the cross-sectional micrograph of an as-received chromized steel sample shown in Fig. 1a [3]. Oxide particles and a layer of thin voids are seen beneath the surface; these are generally acceptable provided they are not interconnecting. Cracks should be absent. Surface-breaking cracks, for example, can provide reactive gaseous species easy access to inner regions of the coatings, where accelerated corrosion may occur. Figure 1b shows the concentration profile of chromium; the coating thickness should

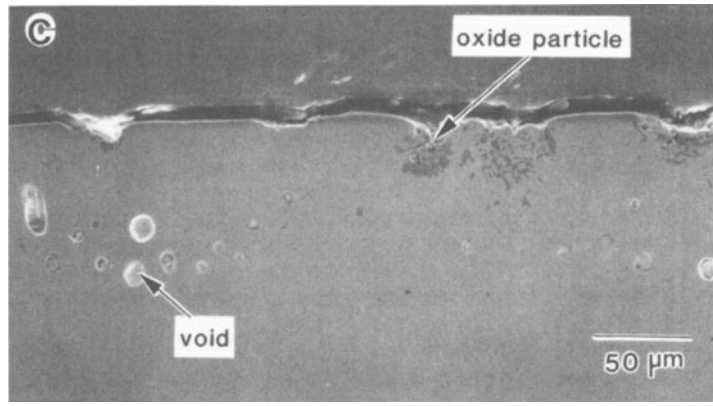

(a)

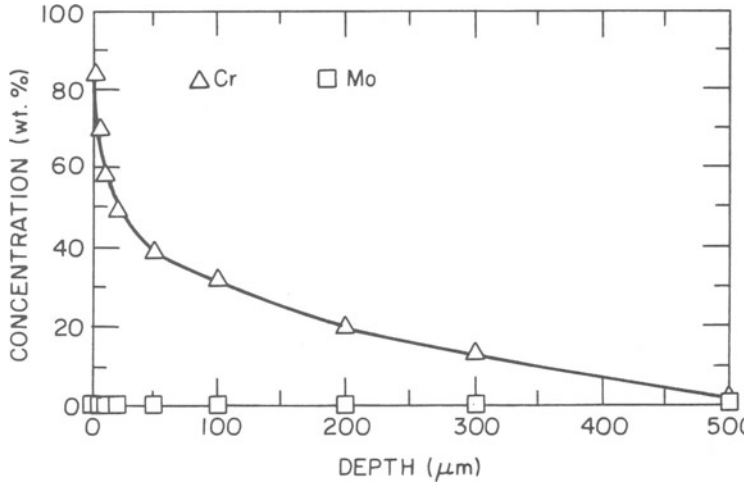

(b)

Fig. 1. (a) Cross-sectional micrograph, and (b) chromium concentration profile of an as-received chromized steel.

be in excess of 200 μm. The coated samples are in the form of 21-mm OD tubes, with surface roughness, in the range of 50-80 μm, that resulted from machining and the pack diffusion process.

The thermal property values of the constituent materials in chrome and chrome-aluminized steels are summarized in Table 1. Using the approach of Bennett and Patty [4], the calculated thermal-wave reflection coefficients at the interface between Cr/steel, Aℓ/Cr, Aℓ/steel, and Cr/air are respectively, 0.06, 0.48, 0.53, and 0.999. Thus the thermal mismatch between Cr and steel in a chromized steel is small compared to that between Aℓ and Cr or Aℓ and steel in a chrome-aluminized steel. This was evident when, early in the project, we subjected these samples to photoacoustic experiments with slanted slots. In these experiments, thermal-wave penetration appeared smaller in chrome-aluminized steel than in chromized steel.

Table 1. Thermal Properties of Constituent Materials in Chrome and Chrome-aluminized Steels

Material	Density (g/cm^3)	Thermal Conductivity (cal/s cm ^oC)	Specific Heat (cal/g ^oC)	Thermal Diffusion Length at 100 Hz (μm)
Aℓ	2.7	2.37	0.215	557
Cr	7.2	0.22	0.110	296
Steel (21 Ni Cr Mo2)	7.8	0.14	0.122	219
Air	1.2×10^{-3}	62.6×10^{-6}	0.240	266

A detailed thermal analysis of these materials is made difficult by (1) the graded nature of the coating (the concentration of the coating element varies with depth), (2) the absence of a clear interface between the coating and the substrate, (3) the presence of a layer of small voids beneath the surface, and (4) surface roughness. Although one could proceed by modeling the coating structure with a multilayer model [5], the validity of such a model would be questionable since the thermal-property changes of the coating with respect to depth are not known. Instead, an experimental determination of the coating-related thermal-wave response can be obtained by normalizing the frequency response of the signals between coated and uncoated samples. Figure 2 shows the normalized photoacoustic magnitude response of a chromized coating, in which the frequency responses of the gas cell, microphone, and lock-in amplifiers used in the data acquisition are cancelled out by dividing the magnitude response of the coated sample by that of an uncoated sample. There appears to be a thermal-wave interference from the coating in the frequency range of 150-400 Hz. A correlation of this result with the coating features, however, remains to be determined.

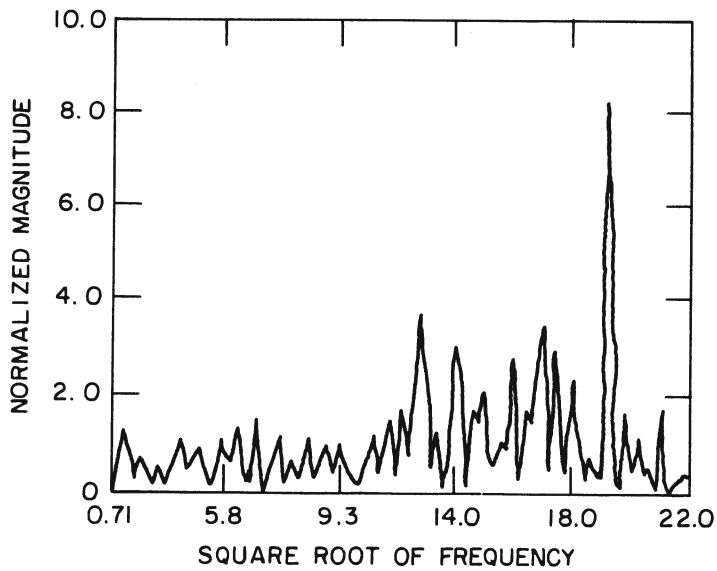

Fig. 2. Normalized thermal-wave response of the chromized coating.

EXPERIMENTAL EVALUATION

The usefulness of the thermal-wave technique for studying these coatings was evaluated under simplified conditions by drilling a slanted (~45°) subsurface hole, as shown in Fig. 3. The drill almost pierced the surface, making a bump on the top. Fortuitously, it also produced a network of fine, surface-breaking cracks on and around the bump. Thus the hole serves as a test bed for both surface and subsurface features.

High Frequency Images

The experimental arrangement used for thermal-wave imaging consists of an acousto-optic modulated Ar^+ laser for generation of thermal waves, a gas cell for detection of thermal waves, and a translation system for point-by-point scanning. Three types of images are produced in each scan: (1) a scanned optical image from specularly reflected light at the sample surface, (2) a photoacoustic magnitude image, and (3) a photoacoustic phase image. Figure 4a shows the thermal-wave images of a 2 x 2-mm bump-containing area at a modulation frequency of 7310 Hz. Details, such as cracks on top of the bump and machining marks on the sample surface, are seen in all three images but show up more clearly in photoacoustic images. In addition, the photoacoustic images show an arc of cracks on the right side of the bump; these cracks are not seen in the scanned optical image.

In the interest of achieving a better signal-to-noise ratio, the laser power was increased to a level where the sample surface was scorched. We were just at the threshold of scorching since, on our curved surface, only the part where the laser was well focused became scorched. An estimate of the power density at which scorching occurred is 2.5 GW/m^2. It is interesting to compare the thermal-wave images before and after scorching. Figure 4b shows 8000-Hz images of the bump area after scorching. A dramatic change is seen in the photoacoustic images of the top of the bump, indicating material damage in this area by laser heating. The arc of cracks on the right side of the bump now also shows up in the scanned optical image because the cracks trap the heat more efficiently, which results in burn marks. Therefore, it appears that if one scans the sample with appropriate laser power, the surface-breaking cracks can easily be detected from the burn marks.

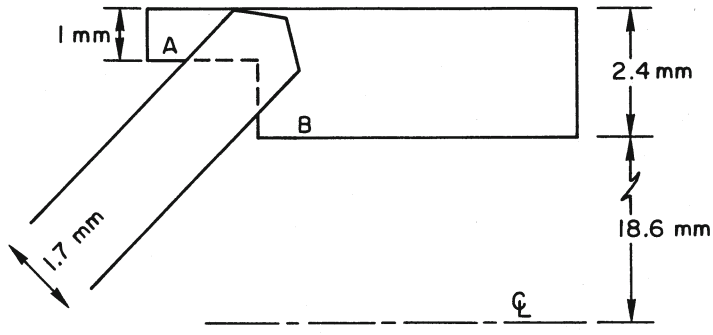

Fig. 3. Drilled subsurface hole ~45°.

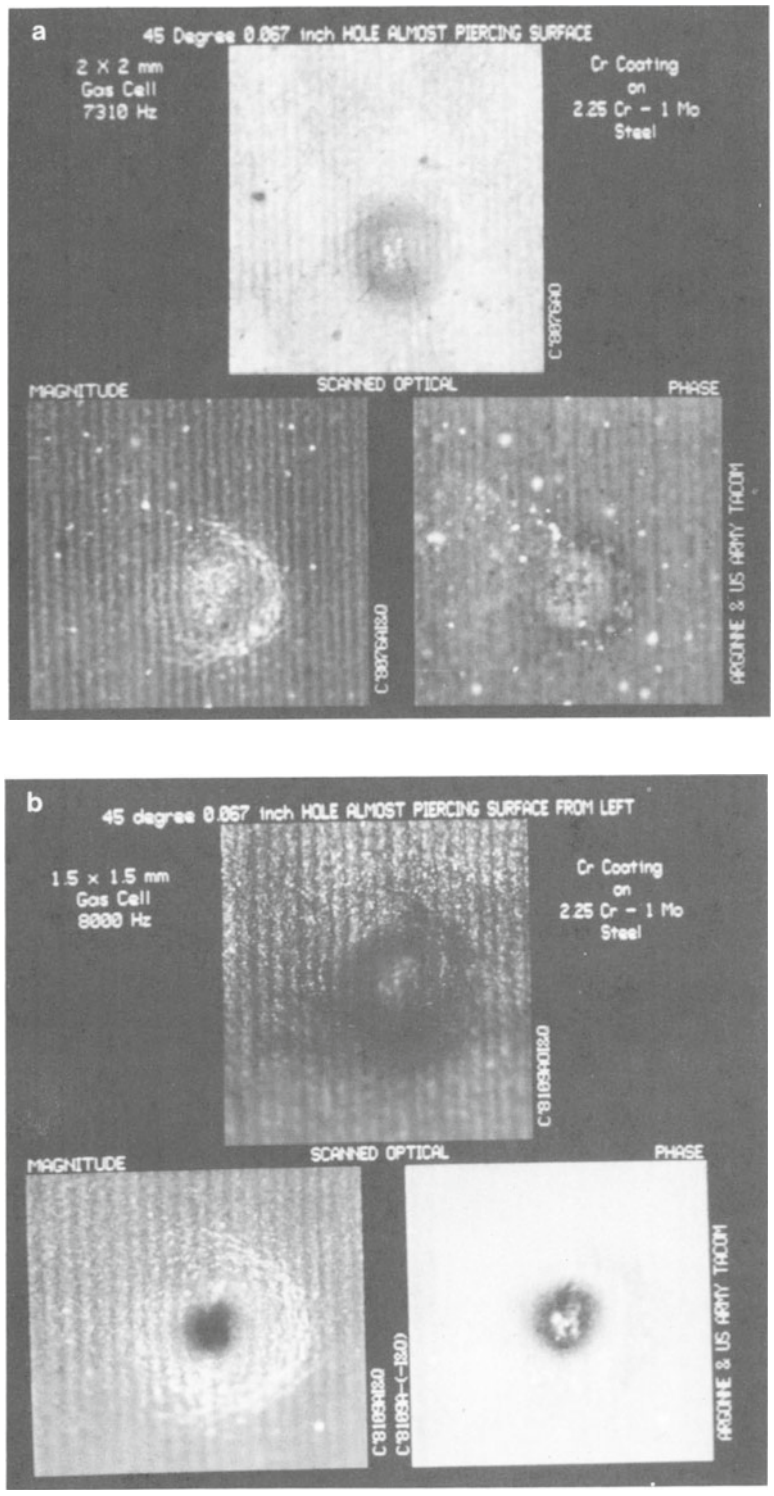

Fig. 4. High-frequency thermal-wave images, (a) before scorching and (b) after scorching.

Low-frequency Images

Since the thermal diffusion length is inversely related to the square root of the modulation frequency, the latter was continually decreased so that the subsurface hole on the left side of the bump could be imaged. Figure 5 shows a series of thermal-wave images at modulation frequencies of 1000, 777, 583, 417, 278, 167, 85, 41, 23.6 and 0.5 Hz. The hole starts showing up on the left side of the bump at approximately 583 Hz and the image of the hole expands progressively as frequency decreases (i.e., as penetration depth increases). Use of frequencies lower than 23.6 Hz resulted in poor signal-to-noise ratios; however, at 0.5 Hz, the brighter region on the left side of the image indicates thermal-wave reflections from the back wall of the 1-mm-thick female joint. As expected, the phase images show more depth of penetration than the magnitude images [6]. The circular fringe pattern seen in the enlarged images is reminiscent of the edge effect [6].

Comparison with an Acoustic Microscopy Image

To correlate the features of the thermal-wave images with the real features of the hole, we must know precisely the relative position, spatial extent, tip orientation, etc., of the hole with respect to the bump. Deferring the destructive testing (sectioning) of the sample, we tested the region of the hole with a 50-MHz acoustic microscope in a pulse-echo mode. Keeping the focal point of the acoustic microscope between the walls A and B of the female joint shown in Fig. 3, we imaged a 4.096 x 3.84-mm area containing the hole. The resultant image is shown in Fig. 6. The hole is shown as a black region in the middle of the picture. The edge joining the walls of the female joint is also shown, with the hole falling on both sides of the edge. In a separate experiment, the hole extended just to the right side of the bump (not shown in the picture). The total horizontal span of the hole area is about 2.1 mm, which agrees with the drawing in Fig. 3. The maximum horizontal span of the hole area in the 23.6-Hz thermal image is only about 1.4 mm. Thus the slanted hole at 23.6 Hz is not seen to its entire depth of 1 mm. At 0.5 Hz, as stated earlier, the thermal wave appears to penetrate the entire 1-mm wall thickness; however, the hole is not well imaged, owing to loss of microphone sensitivity and poor signal-to-noise ratio at such low frequencies. The vertical span of the hole size in the 23.6-Hz thermal images is about 1.7 mm, which agrees with the drawing in Fig. 3. In Fig. 6, the details of the acoustic image away from the horizontal strip of the middle white region are artifacts due to the curved geometry of the sample.

CONCLUSION

This paper reports results obtained from experiments that investigated the use of a thermal-wave technique for evaluating chromized steel tubes. By using a drilled hole, we have established the usefulness of this technique for imaging surface and subsurface features of these coating materials. The use of this technique for deducing the chromium concentration profile in the coating materials requires detailed thermal modeling of the coating structure and knowledge of how the thermal properties of the coating change with depth.

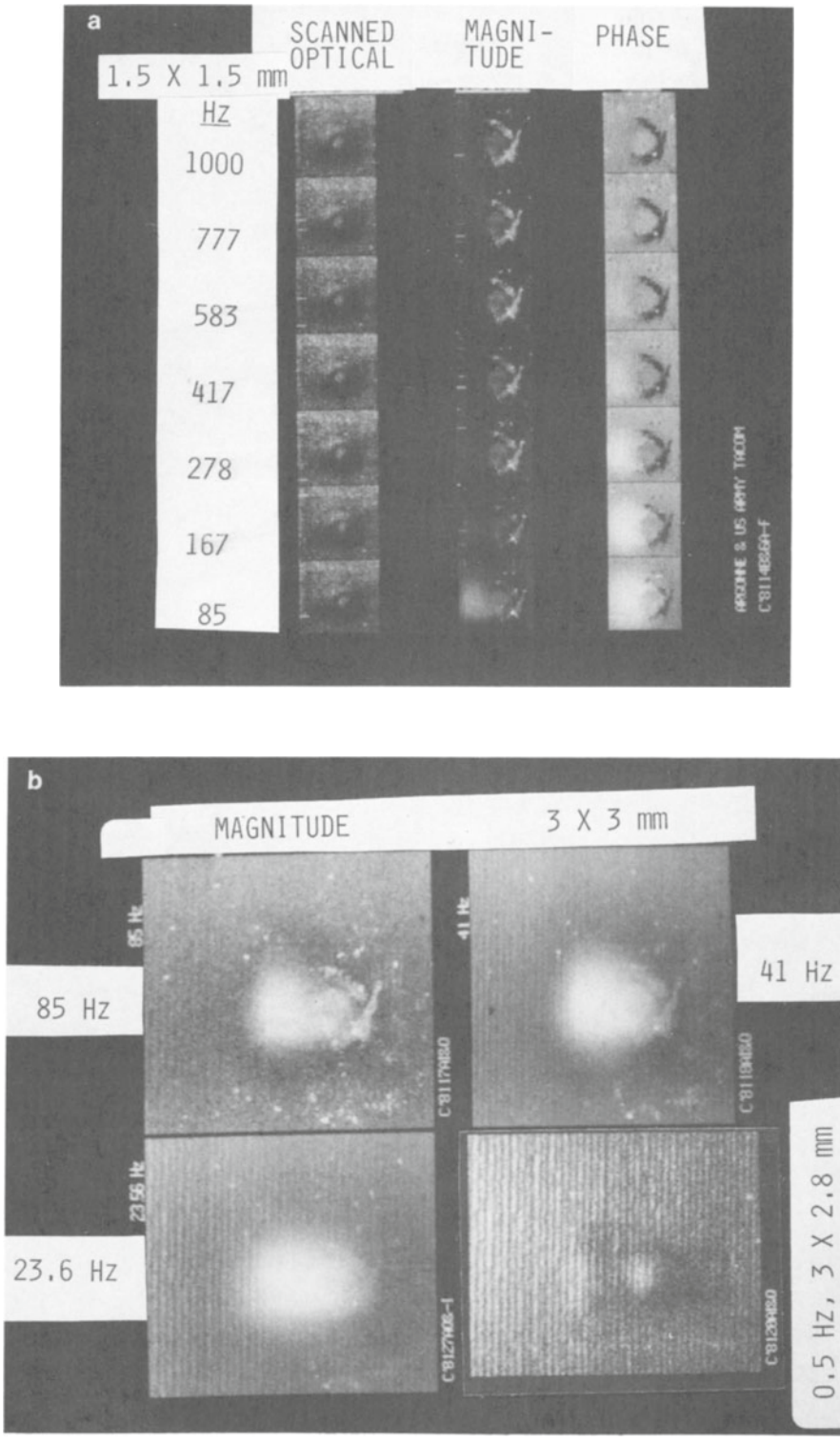

Fig. 5. Sequence of thermal-wave images as the modulation frequency decreases, (a) 1000-85 Hz and (b) 85-0.5 Hz.

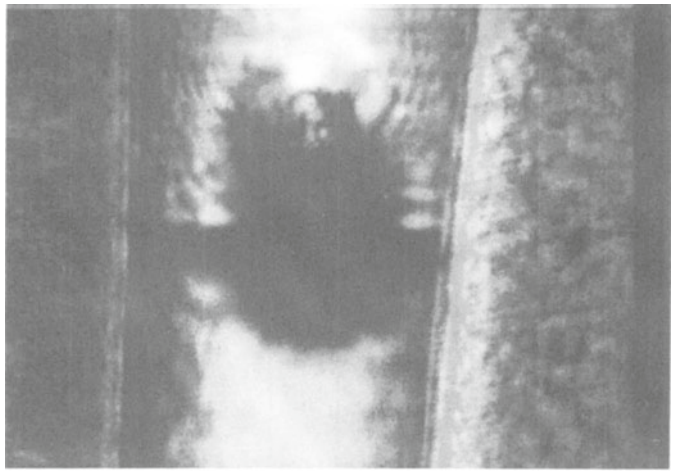

Fig. 6. Acoustic microscopy image of the drilled hole.

ACKNOWLEDGEMENT

This work was supported by the U.S. Department of Energy, Office of Fossil Energy, Morgantown Energy Technology Center, and Oak Ridge Operations Office, as part of the Surface Gasification Materials Program (FWP 49678), under Contract W-31-109-ENG-38.

REFERENCES

1. D. J. Baxter, "The Corrosion Behavior of Coated Low-Alloy Steels in a Coal Gasifier Environment Under Thermal Cycling Conditions," Argonne National Laboratory Report, ANL/FE-86-6 (1986).

2. N. Gopalsami, W. A. Ellingson, R. A. Roberts, and D. N. Rose, "Non-destructive Evaluation of Diffusion Coatings: A Review and Preliminary Results," Argonne National Laboratory Report, ANL/FE-87-7 (1987).

3. D. Wang, "Corrosion Behavior of Chromized and/or Aluminized Cr-Mo Steels in Medium-BTU Coal-Gasifier Environments," Proc. 15th International Conf. on Metallurgical Coatings, April 11-15, 1988, San Diego, CA.

4. C. A. Bennett, Jr., and R. R. Patty, Appl. Opt. 21, 49 (1982).

5. L. C. Aamodt and J. C. Murphy, Can. J. Phy. 64, 1221 (1986).

6. R. L. Thomas, J. J. Pouch, Y. H. Wong, L. D. Favro, and P. K. Kou, J. Appl. Phy. 51, 1152 (1980).